Density-independent plasmons for terahertz-stable topological metamaterials

Jianfeng Wang[a], Xuelei Sui[a,b,c], Wenhui Duan[b,c], Feng Liu[d], and Bing Huang[a,e,1]

[a]Beijing Computational Science Research Center, 100193 Beijing, China; [b]Department of Physics, Tsinghua University, 100084 Beijing, China; [c]State Key Laboratory of Low-Dimensional Quantum Physics, Tsinghua University, 100084 Beijing, China; [d]Department of Materials Science and Engineering, University of Utah, Salt Lake City, UT 84112; and [e]Department of Physics, Beijing Normal University, 100875 Beijing, China

Edited by Angel Rubio, Max Planck Institute for the Structure and Dynamics of Matter, Hamburg, Germany, and approved March 29, 2021 (received for review November 4, 2020)

To efficiently integrate cutting-edge terahertz technology into compact devices, the highly confined terahertz plasmons are attracting intensive attention. Compared to plasmons at visible frequencies in metals, terahertz plasmons, typically in lightly doped semiconductors or graphene, are sensitive to carrier density (*n*) and thus have an easy tunability, which leads to unstable or imprecise terahertz spectra. By deriving a simplified but universal form of plasmon frequencies, here, we reveal a unified mechanism for generating unusual *n*-independent plasmons (DIPs) in all topological states with different dimensions. Remarkably, we predict that terahertz DIPs can be excited in a two-dimensional nodal line and one-dimensional nodal point systems, confirmed by the first-principle calculations on almost all existing topological semimetals with diverse lattice symmetries. Besides *n*-independence, the feature of Fermi velocity and degeneracy factor dependencies in DIPs can be applied to design topological superlattice and multiwalled carbon nanotube metamaterials for broadband terahertz spectroscopy and quantized terahertz plasmons, respectively. Surprisingly, high spatial confinement and quality factor, also insensitive to *n*, can be simultaneously achieved in these terahertz DIPs. Our findings pave the way for developing topological plasmonic devices for stable terahertz applications.

low-dimensional materials | topological semimetals | plasmon | terahertz | electronic structures

Bridging the gap between microwave and infrared regimes, terahertz radiation promises many cutting-edge applications in radar, imaging, biosensing, nondestructive evaluation, and ultrahigh-speed communications (1, 2). While realizing compact terahertz integrated circuits is a big challenge, terahertz plasmons, collective oscillations of electrons at terahertz frequency, provide a revolutionary way to effectively reduce the sizes of terahertz devices down to subwavelength scales (3–8). To achieve highly confined terahertz plasmons, the extensive research has been devoted to various metamaterials, including spoof plasmon polaritons in structured metal surfaces (7–10), terahertz plasmons in lightly doped semiconductors (2, 11–13), and recently developed graphene plasmons (14–16). Compared to the plasmons at visible or ultraviolet (UV) frequency in metals with ultra-high intrinsic charge density (n), the terahertz plasmons (e.g., in doped semiconductors and graphene with ultra-low n) are quite sensitive to the oscillation of n (13–18), as a low n can be greatly changed by the defects (17), thermal fluctuation (2, 16, 19), charge inhomogeneity (20), electrical gating (14, 16, 18), optical excitations (21–23), or charge transfer at interface (Fig. 1*A*). Consequently, their fundamental properties, such as resonance frequency, confinement, and loss of terahertz plasmons (2, 16–18), will be largely affected by the surrounding environments. Therefore, the n-dependence feature leads to unfavorable terahertz applications, such as low temperature limit, high-quality sample requirements, unstable or imprecise terahertz sources, and detection.

It is known that the classical plasmon frequency in conventional electron gas (EG) has an $n^{1/2}$ dependence, while graphene plasmon shows a weaker $n^{1/4}$ power-law scaling (14, 15). Recently, the linear band structures have been extended to a large number of topological semimetals (TSMs) (24, 25), following the fast development of topological matter. Surprisingly, the plasmons with diverse n dependencies have been found in these TSMs even though they have a similar linear band crossing as graphene. For example, the plasmon frequency of three-dimensional (3D) Dirac systems shows $n^{1/3}$ scaling (26), while unconventional n^0-dependent plasmons solely in midinfrared have been found in one-dimensional (1D) metallic carbon nanotubes (CNTs) (27) or 3D nodal-surface electrides (28). Since most previous theories are system dependent, a unified theory to intuitively understand all these plasmonic behaviors in different electronic systems is still lacking, which significantly prevents the design of superior metamaterials for revolutionary terahertz technology and overcoming the intrinsic terahertz-unstable bottlenecks in conventional plasmonic devices.

In this article, we derive a simplified but universal form of plasmon frequencies at a long-wavelength limit that can be applied to understand the collective excitations of all electronic systems with different dimensions. Significantly, a unified mechanism is revealed for generating n-independent plasmons (DIPs), which can be excited in some specific topological states. As demonstrated in Fig. 1*A*, the properties of a DIP, such as its resonance frequency or wavelength, are not affected by the changes of n, which can fundamentally overcome intrinsic terahertz-unstable bottlenecks raised by n-dependent plasmons (DDPs) in conventional systems. Importantly, we predict that the terahertz DIPs can be realized in two reduced systems: two-dimensional (2D) nodal line and 1D nodal point. Extensive first-principle calculations are employed to confirm

Significance

Plasmons, collective electron density oscillations in metals or doped semiconductors, provide an efficient way to couple light and matter at subwavelength scales. Usually, plasmons are carrier density (*n*) dependent, which may cause unstable functionalities of plasmons, especially for cutting-edge terahertz technology. Here, we reveal a unified mechanism for generating unusual *n*-independent plasmons (DIPs), where terahertz DIPs can be excited in some low-dimensional topological semimetals. Stable terahertz spectroscopy from narrowband to broadband and even a quantization can be achieved in topological metamaterials. Our study not only broadens the concept of plasmons by combining with exotic topological states but also paves a way to designing a compact device for stable terahertz applications.

Author contributions: J.W. and B.H. designed research; J.W. and X.S. performed research; J.W., X.S., W.D., F.L., and B.H. analyzed data; and J.W. and B.H. wrote the paper.

The authors declare no competing interest.

This article is a PNAS Direct Submission.

[1]To whom correspondence may be addressed. Email: bing.huang@csrc.ac.cn.

This article contains supporting information online at https://www.pnas.org/lookup/suppl/doi:10.1073/pnas.2023029118/-/DCSupplemental.

Published May 5, 2021.

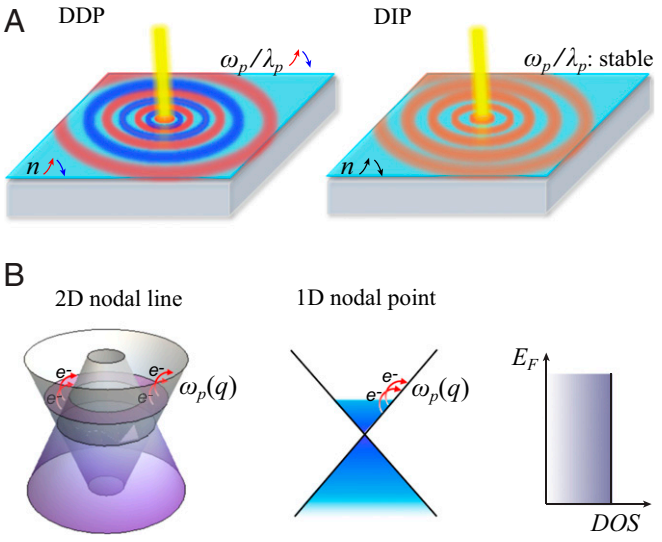

Fig. 1. DIPs and their realizations. (*A*) Schematic comparison between DDP and DIP. Concentric red, blue, or orange circles illustrate plasmon waves excited by electron systems (represented by the cyan plane). For an excited DDP, its resonance frequency (ω_p) or wavelength (λ_p) is sensitive to the oscillation of *n*. When increasing (red arrow) or decreasing (blue arrow) *n*, the ω_p or λ_p of a DDP will increase (red circles) or decrease (blue circles) correspondingly. The properties (ω_p or λ_p) of a DIP (orange circles) are stable against the changes of *n*. (*B*) Linear band structures of 2D nodal line and 1D nodal point and their constant DOS versus E_F. Collective DIPs are labeled schematically by red arrows.

the DIP excitations among 22 known 2D nodal line semimetals (NLSMs) and 1D CNTs. Besides the *n* independence, the frequencies of DIPs can be tuned by Fermi velocity, substrate screening, and degeneracy factor, revealing that a novel, ultrastable terahertz spectrum from narrowband to broadband and a tunable quantization can be achieved in 2D superlattice and 1D multiwalled CNT metamaterials, respectively. Remarkably, stable performance with high spatial confinement and quality factor, critical for device applications, can be simultaneously obtained for terahertz DIPs.

Results

A Unified Mechanism for DIPs. The plasmon excitation can be determined by the dynamical dielectric function $\epsilon(\boldsymbol{q},\omega) = 1 - V(q)\Pi(\boldsymbol{q},\omega)$, where $V(q)$ is dimension-related Coulomb interaction in the wave vector space, and $\Pi(\boldsymbol{q},\omega)$ is the irreducible polarizability function (*Methods*). As a function of Fermi energy (E_F), the key polarizability is usually *n* dependent. Under random phase approximation (RPA) and long-wavelength limit, the *D*-dimensional noninteracting irreducible polarizability near E_F can be approximated by Taylor's first-order expansion (*SI Appendix*, section II):

$$\Pi(\boldsymbol{q},\omega) \approx \frac{g}{(2\pi)^D}\int d^D\boldsymbol{k}\,\frac{\partial n_F}{\partial E}\left(\frac{\partial E}{\partial k}\right)^2\left(\frac{q}{\hbar\omega}\right)^2 \qquad [1]$$

where n_F is the Fermi–Dirac distribution function, and *g* is the degeneracy factor, including degeneracies of spin, valley, and conducting channel. Around $T = 0$ K, we derive, by solving the zeros of dielectric function, a simplified but general form of the plasmon frequency,

$$\omega_p \approx \rho(E_F)^{1/2} v_F V(q)^{1/2} q \qquad [2]$$

,

where $\rho(E_F)$ is the density of states (DOS) of electrons, and $v_F = \hbar^{-1}(\partial E/\partial k)_F$ is the Fermi velocity. Eq. 2, one of our key results, is universal for all dimensional solids, which reveals the most essential elements related to plasmons. Obviously, it shows that, besides $V(q)$, ω_p is mostly determined by DOS and v_F.

Now, we can shed light on the nature of *n* dependence of plasmons for all known systems. For the conventional EGs in metals or doped semiconductors exhibiting a parabolic energy dispersion $E(\boldsymbol{k}) = \hbar^2k^2/2m$, the v_F is E_F (or *n*) dependent. As listed in Table 1, the DOS of conventional EGs is related to their dimensions (*SI Appendix*, section I). Based on Eq. **2**, ω_p of all conventional EGs has a well-known $n^{1/2}$ power-law scaling (Table 1). While all the TSMs have a linear band dispersion, $E(\boldsymbol{k}) = \hbar v_F k$, whose v_F is a constant. In terms of the dimensionality of band crossings, TSMs can be classified into nodal point, nodal line, and nodal surface (24, 25, 29). As demonstrated in Table 1, the ω_p of TSMs has different scalings, solely dependent on their DOS.

As shown in the right column of Table 1, we have rigorously derived the analytical expressions of ω_p for all systems with different dimensions (*Methods* and *SI Appendix*, section II), confirming that Eq. **2** could accurately capture the power-law scaling of ω_p; for example, the $n^{1/4}$ and $n^{1/3}$ DDPs are well reproduced for 2D (e.g., graphene) and 3D nodal point (e.g., Dirac semimetal) systems, respectively. Interestingly, a plasmon with the same *n*-dependent scaling as graphene also appears in 3D nodal line systems, but it has a different anisotropy. In fact, all the analytical expressions in Table 1 can be obtained from Eq. **2** with only a difference of dimensionless coefficient.

Based on Eq. **2**, we can reveal a unified mechanism for realizing a DIP, which needs to meet two general criteria: 1) a constant DOS near E_F and 2) a constant v_F. While 2 can be naturally achieved in the linear band dispersion region of a TSM, 1 is the key criterion for achieving a DIP. After systematic derivations (*SI Appendix*, sections I and II), we conclude that the constant DOS and the resulting DIPs can solely exist in the following TSM states: 3D nodal surface, 2D nodal line, and 1D nodal point, as listed in Table 1. It is noted that the plasmons that occurred in wide parabolic quantum wells (30, 31) can be independent of the electron numbers (not electron density) under certain conditions, which is fundamentally different from our DIPs. We illustrate the constant DOS of 2D nodal line and 1D nodal point in Fig. 1*B*. At long-wavelength limit, the excitation

Table 1. Plasmon frequencies in all dimensions at long-wavelength limit*

	Systems	ρ	$\rho^{1/2}\cdot v_F$	Analytical expression of ω_p
3D	Conventional EG	$E_F^{1/2}(n^{1/3})$	$n^{1/2}$	$\sqrt{\frac{4\pi e^2 n}{\kappa m}}$ (3.1)
	Nodal point	$E_F^2(n^{2/3})$	$n^{1/3}$	$\sqrt{\frac{e^2 v_F}{\kappa\hbar}}\left(\frac{32\pi g}{3}\right)^{1/6} n^{1/3}$ (3.2)
	Nodal line	$E_F(n^{1/2})$	$n^{1/4}$	$\sqrt{\frac{2\pi e^2 v_F}{\kappa\hbar}(1+\sin^2\theta)(g\pi k_0 n)^{1/4}}$ (3.3)
	Nodal surface	$E_F^0(n^0)$	n^0	$\sqrt{\frac{ge^2 v_F \cos^2\theta}{\pi^2\kappa\hbar}}$ (3.4)
2D	Conventional EG	$E_F^0(n^0)$	$n^{1/2}$	$\sqrt{\frac{2\pi e^2 n}{\kappa m}}q^{1/2}$ (3.5)
	Nodal point	$E_F(n^{1/2})$	$n^{1/4}$	$\sqrt{\frac{e^2 v_F}{\kappa\hbar}}(g\pi n)^{1/4}q^{1/2}$ (3.6)
	Nodal line	$E_F^0(n^0)$	n^0	$\sqrt{\frac{ge^2 v_F k_0}{\kappa\hbar}}q^{1/2}$ (3.7)
1D	Conventional EG	$E_F^{-1/2}(n^{-1})$	$n^{1/2}$	$\sqrt{\frac{2e^2 n}{\kappa m}}q\sqrt{\lvert\ln(qa)\rvert}$ (3.8)
	Nodal point	$E_F^0(n^0)$	n^0	$\sqrt{\frac{2ge^2 v_F}{\pi\kappa\hbar}}q\sqrt{\lvert\ln(qa)\rvert}$ (3.9)

See *SI Appendix*, sections I and II for the detailed derivations. Systems exhibiting DIPs are in bold. All conventional EGs have a parabolic dispersion, while all TSMs have a linear dispersion.

*Physical quantities: DOS ρ, Fermi velocity v_F, electron charge *e*, effective mass *m*, background dielectric constant κ, degeneracy factor *g*, size of line (surface) node k_0 (*S*), and lateral confinement size of 1D electron system *a*.

process mainly occurs near E_F. For 2D nodal line, all states involved are in the vicinity of two rings, and the total numbers of their sum will keep a constant when changing E_F (Fig. 1*B*). For 1D nodal point, the total states in the excitations are at two points, and their numbers are also unchanged (Fig. 1*B*). It is noted that all systems are supposed to behave as Fermi liquids, although 1D metallic electrons may also be considered as a Luttinger liquid (32).

As listed in Table 1, the analytical expressions clearly demonstrate the nature of DIPs in 3D nodal surface, 2D nodal line, and 1D nodal point. Besides the n independence, the ω_p is determined by some other physical quantities (i.e., Fermi velocity v_F, degeneracy factor g, and size of degenerate node [k_0 for line node and S for surface node]), giving the tunable factors. Interestingly, the ω_p of all TSMs is manifestly quantum with an explicit "$\hbar$," in contrast to the classical plasmons of conventional EGs (26). In addition, the plasmon dispersion is related to the dimension, which is important for the size effect and spatial compression of plasmons. In order to realize the terahertz metamaterials, we focus on 2D nodal line and 1D nodal point systems [the high DOS prevents the realization of terahertz ω_p in a 3D nodal surface (28)]. The background dielectric constant (κ) of these two systems is determined by the surrounding media, providing another tunable factor of ω_p.

Terahertz DIPs in 2D NLSMs. The 2D NLSMs, having a symmetry-protected crossing between conduction and valence bands along a 1D loop in the Brillouin zone (BZ), attract intensive interests because of their potential applications in quantum devices. Until now, the 2D NLSMs include at least 22 compounds with a wide range of lattice symmetries, such as honeycomb lattice CuSe (33), AgTe (34), and h-B_2O (35); honeycomb-Kagome lattice Hg_3As_2 (36); honeycomb-triangular lattice Cu_2Si (37); Lieb lattice Be_2C (38); and tetragonal lattice X_2Y (X = Ca,Sr,Ba; Y = As,Sb,Bi) (39). These 2D nodal lines are protected by (glide) mirror symmetries. Importantly, all these NLSMs can exhibit the terahertz DIP feature, confirming our unified theory in 2D systems. Here, we take the experimentally synthesized Cu_2Si as an example to demonstrate its DIP excitations, leaving the results of the other 21 compounds in *SI Appendix*, section IV.

As shown in Fig. 2*A*, the monolayer Cu_2Si is composed of a honeycomb Cu lattice and a triangular Si lattice. All Cu and Si atoms are coplaner, and thus a mirror reflection symmetry in respect to the xy plane (M_z) is kept. First, we illustrate the electronic properties of free-standing Cu_2Si. The calculated band structure without spin-orbit coupling (SOC) is shown in Fig. 2*B*. Two band crossings between one conduction band and two valence bands occur along Γ–M and Γ–K lines. Actually, the band crossings take place along two loops in the 2D BZ, as shown in the 2D band plot (Fig. 2*C*). Thus, two concentric nodal lines are formed centered around the Γ point. With opposite eigenstate parities of M_z for the conduction and two valence bands (37), the two nodal lines are protected by mirror reflection symmetry (*SI Appendix*, Fig. S1). Remarkably, the nearly constant DOS is maintained over a large energy range near the Fermi level (Fig. 2*B*), which is the key condition for the formation of DIP excitations in a TSM. After including the SOC effect, the degeneracy of the 2D nodal line is slightly lifted with the appearance of a negligible gap (37) (*SI Appendix*, Fig. S1).

Next, we discuss the plasmon excitation of Cu_2Si. The dynamical dielectric function $\epsilon(\boldsymbol{q},\omega)$ is numerically calculated with 2D Coulomb interaction, $V(q)$, and a background dielectric screening of SiO_2/Si substrate (*Methods*). An electron energy loss spectrum (EELS) is given by the imaginary part of the inverse of $\epsilon(\boldsymbol{q},\omega)$, whose broadened peaks indicate the plasmons (28). As shown in Fig. 2*D*, a 2D plasmon dispersion ($\omega_p \sim q^{1/2}$) is demonstrated; similar to the case of graphene plasmons (40), it lies above the region of intraband electron-hole continuum, indicating that the direct Landau damping is forbidden. Using a typical micrometer wavelength (q = 0.0001 Å^{-1}), we plot the EELS as a function of ω_p and E_F (corresponding to n) in Fig. 2*E*; it shows a clear n-independent feature ($\omega_p \sim n^0$), confirming the existence of DIP. As a comparison, the inset of Fig. 2*E* shows calculated results of graphene plasmon, agreeing well with the experimental data (red circles) (14); the well-known $\omega_p \sim {E_F}^{1/2}$ ($\propto n^{1/4}$) relationship of graphene plasmon is revealed. In addition, the plasmon of Cu_2Si has a significantly larger oscillation strength than that of graphene because of the higher DOS.

At a fixed micrometer wavelength, the plasmon of Cu_2Si stabilizes at a certain THz frequency with high intensity (Fig. 2*E*). As shown in Formula 3.7 in Table 1, the ω_p of 2D nodal line can be tuned by changing Fermi velocity, v_F, and line node size, k_0, which is demonstrated by the strain effect on Cu_2Si (Fig. 2*F* and *SI Appendix*, Fig. S2). The calculated ω_p and $(v_F k_0)^{1/2}$ have a consistent trend, confirming the validity of Formula 3.7. It notes that strain has a small effect on the change of v_F and k_0; consequently, ~5% strain can slightly induce a ~2 THz change of ω_p. On the other hand, ω_p is also sensitive to the background dielectric constant κ (Formula 3.7). As shown in Fig. 2*G*, we further compare the ω_p of Cu_2Si on two substrates, that is, Si(111) and hexagonal boron nitride (h-BN), with quite different κ. Importantly, the nodal lines can survive on both substrates (*SI Appendix*, Fig. S3). Interestingly, a threefold frequency change, from terahertz to midinfrared, can be achieved by simply changing the underneath substrate of Cu_2Si.

A Broadband Terahertz Spectroscopy in 2D NLSM Metamaterials. The intrinsic properties of nodal line (e.g., v_F and k_0) are material dependent, indicating that a broad range of DIPs with different ω_p may be achieved by the choice of different TSMs. Indeed, the DIP features are not only confirmed in all other NLSMs (*SI Appendix*, Figs. S4–S11) but also exhibit a broad range from 4 THz (in Ca_2As) to 16 THz (in h-B_2O) (Fig. 3*A* and *SI Appendix*, Table S2). Once again, the ω_p obtained from Formula 3.7 fits well with the first-principle results independent of their diverse lattice symmetries, except for the case of h-B_2O, which is due to the strong anisotropy of its nodal line (35) (*SI Appendix*, Fig. S7).

Recently, the development of 2D van der Waals (vdW) heterostructures enables manipulating crystals for exploration of physics not observable in conventional materials (41, 42). Employing the heterostructures (or superlattice) of 2D NLSMs, here, a novel ultrastable terahertz metamaterial device can be proposed, as drawn in Fig. 3*B*. For vdW stackings of 2D NLSMs, a compensation momentum is necessary for incident light, which can be realized in the scattering-type scanning near-field optical microscopy (s-SNOM) technology (16, 27). The 2D NLSMs can also be fabricated in microribbon arrays on transparent substrates (14); thus, a grating superlattice can be well-designed by stacking them layer by layer (Fig. 3*B*). Determined by the selections of fabricated NLSMs, ribbon/gap width, and even substrates, multiple terahertz-frequency plasmons can be simultaneously excited. For instance, one can adopt the same or different materials/pattern periods for fabrications. Thus, a terahertz spectroscopy from narrowband to broadband can be achieved. Most importantly, the spectroscopy in such a device could be ultrastable under the variable environments against charge doping. Our proposed device can be used as an ultrastable terahertz signal amplifier or an ultrastable terahertz sensor, which could selectively output or detect multiband terahertz waves.

Terahertz DIPs in 1D CNTs. The nodal point semimetals have been widely studied (e.g., Dirac points in 2D graphene or 3D Na_3Bi) (25). To confirm our DIP model in 1D nodal point systems (Formula 3.9 in Table 1), armchair CNTs have been selected as typical examples, as they are known as 1D Dirac-point semimetals (43).

The structure and 1D Dirac bands of armchair CNTs are shown in *SI Appendix*, Fig. S12. The calculations of (5, 5), (10, 10), and

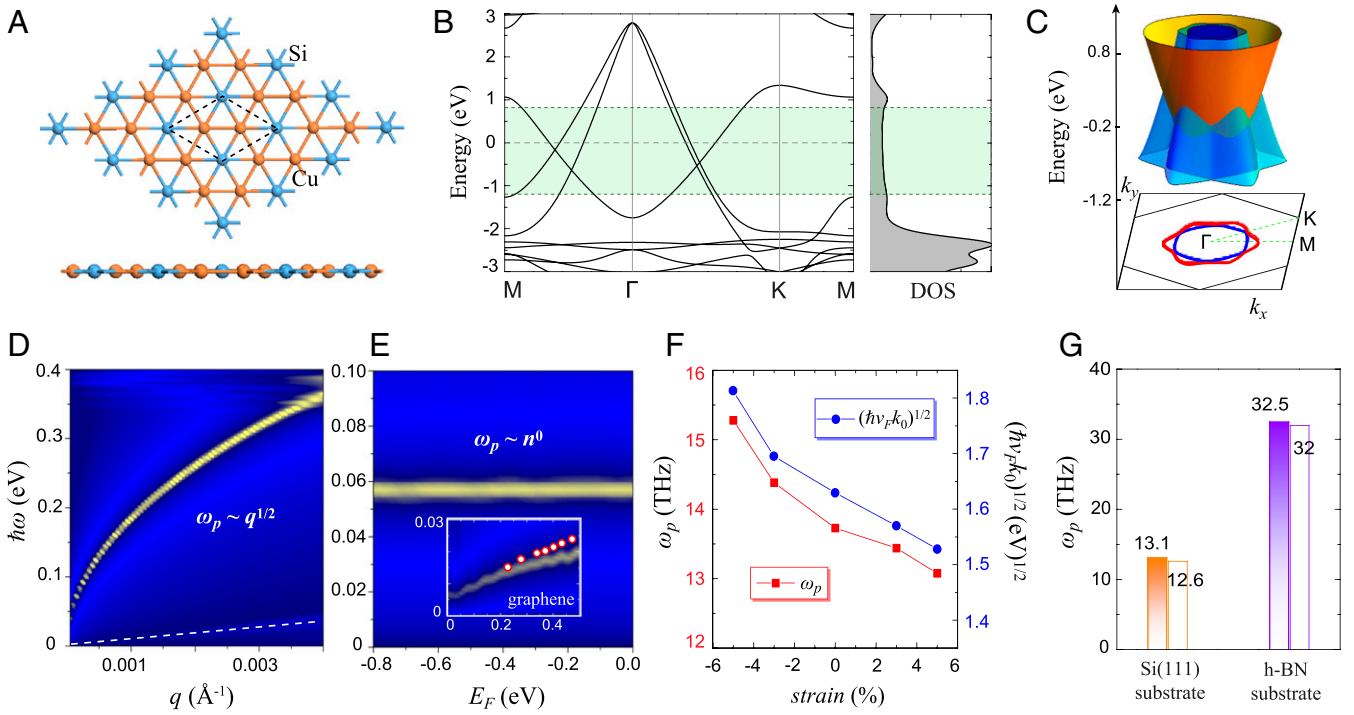

Fig. 2. DIP in 2D NLSM Cu_2Si. (*A*) Top and side views of monolayer Cu_2Si. Black rhombus depicts primitive cell. (*B*) Calculated band structure and DOS (without SOC) for Cu_2Si. Fermi level is set to zero. (*C*) 3D plot of 2D bands in the energy range from −1.2 to 0.8 eV (green region in *B*). Band crossings between conduction and two valence bands are projected to the 2D BZ (red and blue loops). (*D*) EELS as a function of frequency and wave vector. The white dashed line denotes the upper edge $\hbar v_F q$ of intraband particle-hole continuum. (*E*) EELS as a function of frequency and Fermi energy (q = 0.0001 Å^{-1}). (*Inset*) EELS of graphene plasmon with the same calculation parameters as Cu_2Si. Experimental data of graphene (14) are marked as red circles (their brightness indicates the plasmon oscillation strength). (*F*) Calculated plasmon frequency and related physical quantities obtained from band structures under strain. (*G*) Plasmon frequency with two different substrates. Solid columns: numerical results from first principles; hollow columns: analytical results calculated from Formula 3.7 in Table 1.

(15, 15) nanotubes reveal that the v_F of Dirac electrons are almost independent of their tube diameters a and all of them have a constant DOS near the Fermi level (*SI Appendix*, Fig. S12). Using 1D Coulomb interaction and a BN substrate dielectric screening (*Methods*), the $\epsilon(q, \omega)$ and EELS of these CNTs can be obtained. As shown in Fig. 4*A*, the plasmon dispersion of (5, 5) nanotube demonstrates a typical 1D feature ($\omega \sim |q|$ at long wavelength). It also lies above the region of intraband electron-hole continuum without direct Landau damping. With a micrometer wavelength (q = 0.0001 Å^{-1}), the EELS as a function of ω_p and E_F (corresponding to n) for (5, 5) and (10, 10) nanotubes is calculated, as shown in Fig. 4*B*. Remarkably, the terahertz DIP feature ($\omega_p \sim n^0$) is revealed for both CNTs, and the ω_p calculated from first principles are consistent with the analytical results (red dashed lines in Fig. 4*B*). Moreover, the ω_p of CNTs are almost a independent as a result of the weak a-dependent v_F (i.e., there is only a weak logarithm dependence on the diameter of CNTs) (44) (see Formula 3.9 in Table 1). Interestingly, the recent experimental observations on metallic nanotubes with different diameters confirm the existence of midinfrared DIPs (27). Our results are in good agreement with the experimental measurements (red triangles in Fig. 4*A*), also reflecting the weak a dependence.

Quantized Terahertz Plasmons in 1D CNT Metamaterials. In terms of Formula 3.9, the weak a dependence indicates that ω_p of CNTs is mostly determined by the degeneracy factor g. In multiwalled nanotubes (MWNT), the Dirac points could maintain due to the weak vdW interactions between the individual tubes (*SI Appendix*, Fig. S12); meanwhile, the long-range Coulomb interactions make conducting channels of electrons determined by the number of walls (N_w). Thus, we propose that a quantized terahertz, ω_p, may be achieved in MWNT metamaterials. As shown in Fig. 4*B*, the calculated plasmon excitations of (5, 5)@(10, 10) double-walled nanotubes and (5, 5)@(10, 10)@(15, 15) triple-walled nanotubes are demonstrated. Interestingly, besides the DIP feature, the ω_p of MWNT can exhibit a clear, quantized plateau as a function of N_w, as shown in Fig. 4*C*. It notes that a similar quantization of propagation velocity has been observed in single-walled CNT bundles (27), explained by a many-body Luttinger liquid theory. Importantly, differing from the previous theory (27), the emergence of quantized ω_p comes naturally from our unified DIP theory in 1D system (Formula 3.9). Therefore, a quantized manipulation of ultrastable teraherz plasmons using a series of MWNT can be well designed (Fig. 4*D*) (e.g., discrete frequencies or wavelengths can be excited at different thickness of a telescoping MWNT). Meanwhile, an s-SNOM technology may be needed (16, 27).

Spatial Confinement and Lifetime of Terahertz DIPs. As two important figures of merit for plasmonics, spatial confinement and quality factor are also calculated for the DIPs in 2D NLSMs and 1D CNTs in comparison to graphene plasmon (Fig. 5 and *SI Appendix*, Fig. S13). The spatial confinement, defined as the ratio of free-space light wavelength and plasmon wavelength (λ_0/λ_p), is found to be related to the dimensions; when increasing the ω_p, it can be enhanced for 2D systems but almost unchanged for 1D plasmons, consistent with the theoretical derivations (Fig. 5*A* and *SI Appendix*, section VII). Strong confinement effect is available for terahertz DIPs [e.g., in (5, 5) CNTs and Ca_2As] (Fig. 5*A*), which is critical for the design of compact devices. The quality factor (Q), measuring the number of oscillating cycles a plasmon can propagate, is related to the plasmonic damping rate or lifetime. Due to the forbidden or weak direct Landau damping, the phonon-assisted damping rate of plasmons is solely considered (*Methods*). The calculated lifetimes (τ_p) can reach tens of picoseconds at low ω_p but reduce rapidly when ω_p increases to the frequency of optical phonons (Fig. 5*B*).

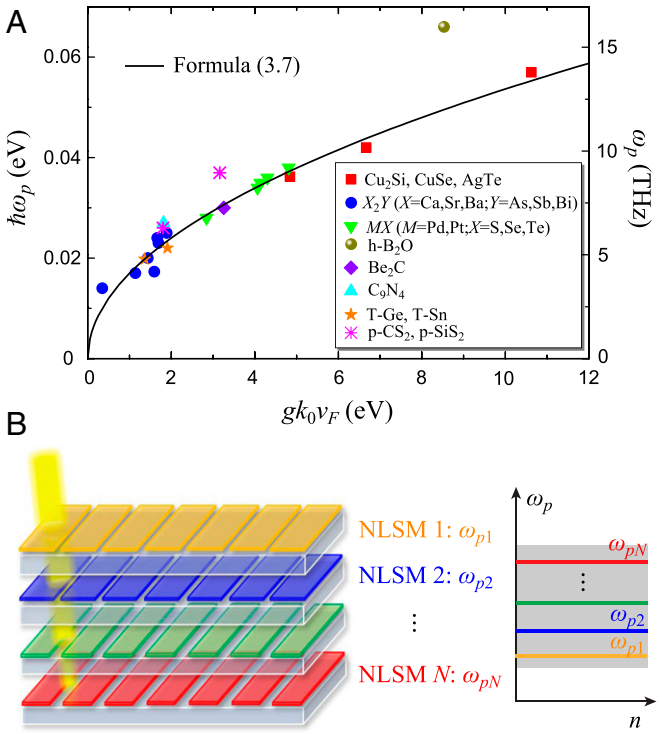

Fig. 3. DIPs in 2D NLSM metamaterials for ultrastable and broadband terahertz spectroscopy. (*A*) Plasmon frequency as a function of gk_0v_F for 22 2D NLSMs, where q = 0.0001 Å^{-1} and SiO_2/Si substrate are adopted (*Methods*). The 22 colored points: numerical results obtained from first principles; black curve: analytical results obtained from Formula 3.7 in Table 1. (*B*) vdW heterostructures or grating superlattice of 2D NLSMs for ultrastable terahertz spectroscopy. For grating superlattice, transparent substrates are needed.

Usually, strong spatial confinement of a plasmon is achieved at the expense of a low quality factor for metals. Remarkably, the calculated midinfrared graphene plasmon (e.g., at 30 THz) could simultaneously exhibit extraordinary spatial confinement $\lambda_0/\lambda_p \sim 105$ and high quality factor ($Q \sim 360$), consistent with the experimental observations (16). Intererstingly, the simultaneous high spatial confinement and quality factor can be also achieved in terahertz DIPs, such as $\lambda_0/\lambda_p \sim 13$(66), $Q \sim 15$ (67) for plasmon in Ca_2As (CNT) at 3 (10) THz. As shown in Fig. 5*C*, the performance (λ_0/λ_p and τ_p) of graphene plasmons can be greatly affected by the charge doping, which is also demonstrated in a recent experiment (18). However, for terahertz DIPs, these figures of merit are robust against the change of n (Fig. 5*C*), revealing that the n-independent feature of DIPs also benefits their device performance.

Discussion

For 2D NLSMs, some of them have been synthesized on metal substrates (33, 34, 37). Although the mirror reflection symmetry is broken considering the different media of vacuum and substrate, the nodal lines survive due to the weak substrate–overlayer interactions (37). Because of the significantly different excitation regions of ω_p in these NLSMs (terahertz) and their metal substrates (UV), we expect that the novel DIPs are ready to be detected in the experiments. It is also expected that they can further be deposited on insulating substrates (such as SiO_2/Si or BN) by the transfer technique (42) for better optical measurements, where near-field optical microscope (16, 27) or lithography and etching technologies (14) may need to be adopted. Meanwhile, some other 2D NLSMs are expected to be synthesized or exfoliated from their bulk materials. For 1D nodal point TSMs, the large-scale, high-quality CNTs can be synthesized in the experiments (45).

It is noted that although some metallic 2D materials [e.g., TaS_2 (46, 47)] may also have nearly linear band dispersion around E_F, the DOS is still nonconstant, making their plasmons n dependent (*SI Appendix*, Fig. S14). It is also highlighted that all the theories and models are based on the RPA and long-wavelength limit, beyond which the features of DIPs may no longer exist (*SI Appendix*, Fig. S15). In addition, although for conventional metals with a sizeable equilibrium n, their plasmon can also demonstrate a weak n dependence due to the relatively small change of n in reality, this situation is not included in our unified mechanism for realizing DIP, since for the terahertz plasmons, the realistic change of n can be comparable to equilibrium n (*SI Appendix*, section X).

Our study has significant impacts in multiple fields. First, a unified model or general form of plasmon frequency (Eq. **2**) for all electronic systems in different dimensions is derived, which could capture the most fundamental features of plasmons. Importantly, a universal mechanism for realizing a DIP is devised, shedding important insights in understanding the DIPs excited in the 2D nodal line systems as well as 3D nodal-surface (28) and 1D nodal-point (27, 44, 48) systems. Second, new terahertz metamaterials based on a large number of TSMs are designed to achieve a terahertz-stable spectroscopy from narrowband to broadband or a quantized manipulation of terahertz frequencies. All these results, together with simultaneous high spatial confinement and quality factor for terahertz DIPs, can be ready to be applied in compact terahertz devices with high stability and precision, such as ultrastable signal amplification and accurate detection. Therefore, our work paves the way to developing exotic plasmonic applications in nanophotonic and nanophotoelectric devices, which may potentially open a field for terahertz-stable plasmonics and related technologies.

Methods

First-Principles Calculations. The first-principles calculations are performed using the Vienna ab initio simulation package (49) within the projector augmented wave method (50) and the generalized gradient approximation of the Perdew–Burke–Ernzerhof (51) exchange-correlation functional. The Γ-centered k-point meshes are adopted. Fixing the crystal symmetry, the structures from experiments or literatures are relaxed until the residual forces on each atom is less than 0.01 eV/Å. The thickness of vacuum is taken to be 18 Å, which is adequate to simulate 2D or 1D materials. Cu_2Si has a lattice constant of 4.123 Å, and the crystal structures of other materials can be found in *SI Appendix*. SOC is also considered in part of our calculations. A tight-binding (TB) Hamiltonian based on the maximally localized Wannier functions (MLWF) (52) is constructed to get the energy eigenvalues and eigenstates for further dielectric function calculations.

Plasmon Calculations. The plasmon excitation can be determined by

$$\epsilon(\boldsymbol{q},\omega) = 1 - V(q)\Pi(\boldsymbol{q},\omega) = 0\,, \qquad [4]$$

where $\epsilon(\boldsymbol{q},\omega)$, a function of the wave vector $\boldsymbol{q}$ and frequency ω, is the dynamical dielectric function. $V(q)$ is the D-dimensional Coulomb interaction in the wave vector space (26):

$$V(q) = \begin{cases} 4\pi e^2/\kappa q^2, (D=3) \\ 2\pi e^2/\kappa q, (D=2) \\ 2e^2|\ln(qa)|/\kappa. (D=1)\,. \end{cases} \qquad [5]$$

$\kappa = 4\pi\epsilon_0\epsilon_r$ is the background dielectric constant, where ϵ_0 and ϵ_r are the vacuum and background relative dielectric constants, respectively. $\Pi(\boldsymbol{q},\omega)$ is the irreducible polarizability function. Under RPA and long-wavelength limit ($q \to 0$), the plasmon frequency in a D-dimensional electron system can be determined by a noninteracting irreducible polarizability (26, 28),

$$\Pi(\boldsymbol{q},\omega) = \frac{g}{(2\pi)^D}\int d^D\boldsymbol{k}\sum_{l,l'}\frac{n_F(E_{\boldsymbol{k},l}) - n_F(E_{\boldsymbol{k}+\boldsymbol{q},l'})}{\hbar\omega + E_{\boldsymbol{k},l} - E_{\boldsymbol{k}+\boldsymbol{q},l'} + i\eta}F_{ll'}(\boldsymbol{k},\boldsymbol{q})\,, \qquad [6]$$

in which n_F is the Fermi–Dirac distribution function, and $F_{ll'}(\boldsymbol{k},\boldsymbol{q})$ is the overlap form factor $\left|\langle \boldsymbol{k}+\boldsymbol{q}, l'|e^{i\boldsymbol{q}\cdot\boldsymbol{r}}|\boldsymbol{k}, l\rangle\right|^2$ with $|\boldsymbol{k}, l\rangle$ and $E_{\boldsymbol{k},l}$, the eigenstate and

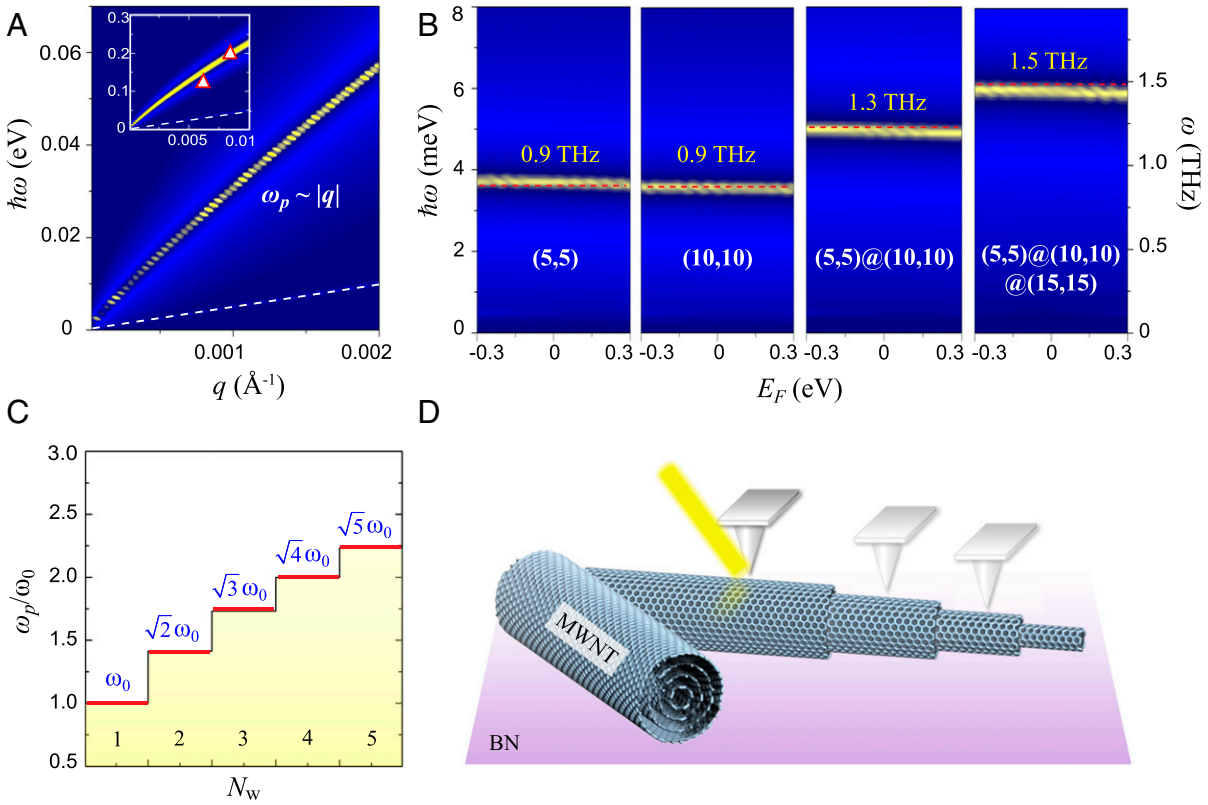

Fig. 4. Terahertz DIPs in 1D metallic CNTs and their quantization. (*A*) EELS as a function of frequency and wave vector. The white dashed line denotes the upper edge $\hbar v_F q$ of intraband particle-hole continuum. (*Inset*) EELS at a large scale of wave vector. Red triangles: experimental data adopted from ref. 27. (*B*) EELS as a function of frequency and Fermi energy for two different single-, (5, 5)-@-(10, 10) double-, and (5, 5)-@-(10, 10)-@-(15, 15) triple-walled nanotubes (q = 0.0001 Å^{-1}). Red dashed lines: analytical results from Formula 3.9 in Table 1. (*C*) A quantized DIP frequency as a function of the number of walls (N_w) in MWNT. (*D*) Schematic plot of 1D MWNT metamaterial for an ultrastable terahertz spectroscopy with tunable and quantized frequencies.

energy dispersion, respectively. The factor g in Eq. **6** is the degeneracy factor, including degeneracies of spin, valley, and conducting channel, and η is related to the electron lifetime due to the damping. The zeros of complex dielectric function signify a self-sustaining collective mode and give the plasmon frequency.

Numerical calculations. The energy eigenvalues and eigenstates in Eq. **6** are obtained from the TB Hamiltonian of MLWF. The integral is over the first BZ, where a temperature of 300 K in the Fermi–Dirac distribution function and an infinitesimal broadening η = 1 meV are used. Considering the spin degree of freedom, the degeneracy factor g is set to 2 in the numerical calculations of all systems, while in theoretically derived formula in Table 1, g should be adopted as 4 for Cu_2Si, CuSe, and AgTe because of the two nodal lines in these three TSMs and 4 (6) for double-walled nanotubes (triple-walled nanotubes). For $V(q)$, the relative dielectric constant is determined by $\epsilon_r = (\epsilon_0 + \epsilon_{sub})/2$ for 2D and 1D systems, representing the effective dielectric function of environments (vacuum and substrate). For a SiO_2/Si substrate, ϵ_r = 5 (14); for a BN substrate, ϵ_r = 1 (27). In the 1D Coulomb interaction, a is the lateral confinement size of a 1D electron system (e.g., the diameter of

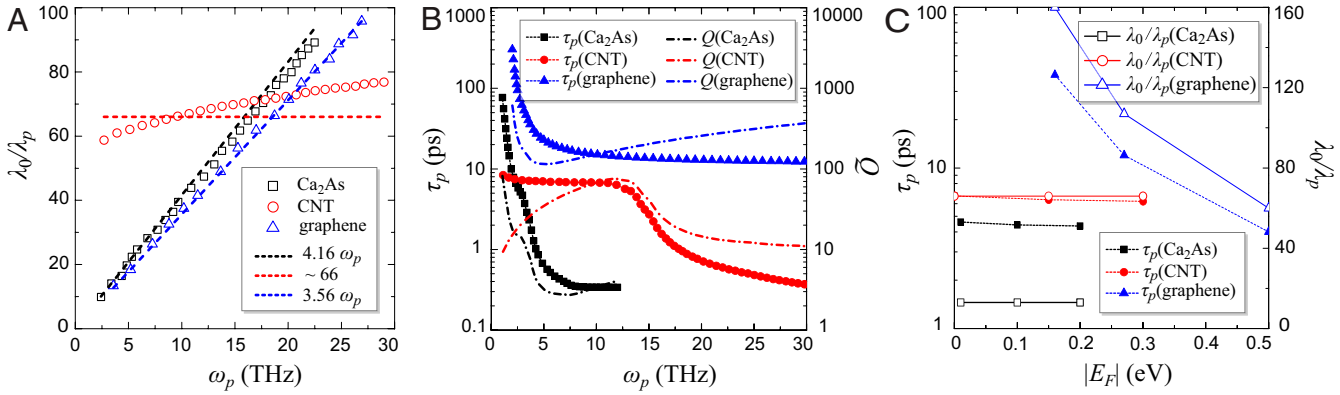

Fig. 5. Spatial confinement and lifetime of DIPs. (*A*) Spatial confinement (λ_0/λ_p) as a function of ω_p for Ca_2As, (5, 5) CNT, and graphene. The dashed lines are theoretically derived λ_0/λ_p for the three systems (*SI Appendix*, section VII). E_F = 0.27 eV is adopted for graphene in order to compare with experiment (16). (*B*) Lifetime (τ_p) and quality factor (Q) as functions of ω_p for Ca_2As, CNT, and graphene. (*C*) λ_0/λ_p and τ_p as functions of $|E_F|$ for Ca_2As, CNT, and graphene. The ω_p is fixed at 3, 10, and 30 THz for Ca_2As, CNT, and graphene, respectively.

nanotubes). When studying the density dependence of plasmon, we have fixed the wave vector as $q = 0.0001$ Å^{-1}, which corresponds to a typical micrometer wavelength easily available in experiments (14).

The collective plasmon mode is defined at zeros of Eq. **4**. In general, the dielectric function is a complex functional. The complex solution at $\epsilon(\boldsymbol{q}, \omega) = 0$ gives both the plasmon dispersion (real part) and the decay of the plasmon (imaginary part). In order to compare with the experiments, it is more convenient to calculate the EELS, whose broadened peaks indicate the plasmons (28);

$$\mathrm{EELS} = -\mathrm{Im}\left[1/\epsilon(\boldsymbol{q}, \omega)\right] . \quad [7]$$

Analytical derivations. In the analytical derivations of ω_p, only the intraband excitations are considered. $E(\boldsymbol{k}) = \hbar^2 k^2/2m$ and $E(\boldsymbol{k}) = \hbar v_F k$ are employed for conventional EGs and TSMs, respectively. The overlap form factor is $F(\boldsymbol{k}, \boldsymbol{q}) = 1$, and a Fermi–Dirac distribution function with 0 K is adopted. The detailed derivations for all systems are shown in *SI Appendix*. The final results are summarized in the right column of Table 1. In comparison with the results of numerical calculations, the degeneracy factor g should be adopted as 4 for Cu_2Si, CuSe, and AgTe because of the two nodal lines in these three TSMs, 4 (6) for double-walled nanotubes (triple-walled nanotubes), and 2 for other materials.

Calculations of Plasmon Lifetime. The phonon-assisted damping rate of plasmons is only considered due to the forbidden or weak direct Landau damping in the studied systems at a long-wavelength limit. The plasmon lifetime can be determined from the alternating current conductivity, which is related to the transport relaxation time (τ_{tr}) (53). The transport scattering rate can be written as (53)

$$\frac{1}{\tau_{tr}} = \frac{2\pi}{\omega}\int_0^{\omega} d\omega' \left(\omega - \omega'\right)\alpha_{tr}^2 F\left(\omega'\right) . \quad [8]$$

$\alpha_{tr}^2 F$ is a transport related Eliashberg spectral function, and it is defined as

$$\alpha_{tr}^2 F(\omega) = \frac{1}{2N_F}\sum_{\boldsymbol{k}\boldsymbol{q}\nu} |g^{\nu}(\boldsymbol{k}, \boldsymbol{q})|^2 \left(-\frac{\boldsymbol{q}\cdot\boldsymbol{k}}{k^2}\right)\delta(\varepsilon_{\boldsymbol{k}} - \varepsilon_F)\delta(\varepsilon_{\boldsymbol{k}+\boldsymbol{q}} - \varepsilon_F)\delta(\omega - \omega_{\boldsymbol{q}\nu}) . \quad [9]$$

where $g^{\nu}(\boldsymbol{k}, \boldsymbol{q})$ is the electron–phonon (*e-ph*) matrix element. It quantifies a scattering process from an initial Bloch state $|n\boldsymbol{k}\rangle$ (with band n and momentum $\boldsymbol{k}$) to a final state $|m\boldsymbol{k} + \boldsymbol{q}\rangle$ by emitting or absorbing a phonon with wavevector $\boldsymbol{q}$, mode index ν, and frequency $\omega_{\nu\boldsymbol{q}}$,

$$g_{nm\nu}(\boldsymbol{k}, \boldsymbol{q}) = \frac{1}{\sqrt{2\omega_{\nu\boldsymbol{q}}}}\langle m\boldsymbol{k} + \boldsymbol{q}|\partial_{\boldsymbol{q}\nu} V|n\boldsymbol{k}\rangle , \quad [10]$$

where $\partial_{\boldsymbol{q}\nu} V$ is the derivative of the self-consistent potential.

The *e-ph* coupling matrix elements can be computed within the density-functional perturbation theory. Here, a Wannier–Fourier interpolation method, as implemented in the EPW (electron–phonon coupling using Wannier functions) code (54) and integrated in the Quantum ESPRESSO package (55), is used to obtain the numerical results of *e-ph* coupling. The electron eigenstate and eigenvalue vibrational modes and frequencies as well as *e-ph* matrix elements that are first calculated on a relatively coarse BZ grid and then Wannier-interpolated values on a fine grid are obtained.

Data Availability. All study data are included in the article and/or *SI Appendix*.

ACKNOWLEDGMENTS. We thank L. Kang and Z. Wang for helpful discussions. J.W. and B.H. acknowledge support from National Natural Science Foundation of China (NSFC) (Grant Nos. 11634003, 12088101, 12004030, and 11704023) and NSAF U1930402. X.S. and W.D. acknowledge support from Ministry of Science and Technology (MOST) of China (Grant No. 2016YFA0301001), NSFC (Grant Nos. 11674188 and 11874035), and the Beijing Advanced Innovation Center for Future Chip. F.L. acknowledges support from US Department of Energy (Grant No. DE-FG02-04ER46148). Part of the calculations were performed at Tianhe2-JK at Computational Science Research Center.

1. M. Tonouchi, Cutting-edge terahertz technology. *Nat. Photonics* **1**, 97–105 (2007).
2. D. Saeedkia, *Handbook of Terahertz Technology for Imaging, Sensing and Communications* (Woodhead Publishing Limited, Cambridge, UK, 2013).
3. S. A. Maier, *Plasmonics: Fundamentals and Applications* (Springer, New York, 2007).
4. W. L. Barnes, A. Dereux, T. W. Ebbesen, Surface plasmon subwavelength optics. *Nature* **424**, 824–830 (2003).
5. H.-T. Chen *et al.*, Active terahertz metamaterial devices. *Nature* **444**, 597–600 (2006).
6. N. I. Zheludev, Y. S. Kivshar, From metamaterials to metadevices. *Nat. Mater.* **11**, 917–924 (2012).
7. N. Yu *et al.*, Terahertz plasmonics. *Electron. Lett.* **46**, S52–S57 (2010).
8. X. Zhang *et al.*, Terahertz surface plasmonic waves: A review. *Adv. Photonics* **2**, 014001 (2020).
9. J. B. Pendry, L. Martín-Moreno, F. J. García-Vidal, Mimicking surface plasmons with structured surfaces. *Science* **305**, 847–848 (2004).
10. C. R. Williams *et al.*, Highly confined guiding of terahertz surface plasmon polaritons on structured metal surfaces. *Nat. Photonics* **2**, 175–179 (2008).
11. S. J. Allen, D. C. Tsui, R. A. Logan, Observation of the two-dimensional plasmon in silicon inversion layers. *Phys. Rev. Lett.* **38**, 980–983 (1977).
12. G. C. Dyer *et al.*, Induced transparency by coupling of Tamm and defect states in tunable terahertz plasmonic crystals. *Nat. Photonics* **7**, 925–930 (2013).
13. I. Kriegel, F. Scotognella, L. Manna, Plasmonic doped semiconductor nanocrystals: Properties, fabrication, applications and perspectives. *Phys. Rep.* **674**, 1–52 (2017).
14. L. Ju *et al.*, Graphene plasmonics for tunable terahertz metamaterials. *Nat. Nanotechnol.* **6**, 630–634 (2011).
15. A. N. Grigorenko, M. Polini, K. S. Novoselov, Graphene plasmonics. *Nat. Photonics* **6**, 749–758 (2012).
16. G. X. Ni *et al.*, Fundamental limits to graphene plasmonics. *Nature* **557**, 530–533 (2018).
17. J. M. Luther, P. K. Jain, T. Ewers, A. P. Alivisatos, Localized surface plasmon resonances arising from free carriers in doped quantum dots. *Nat. Mater.* **10**, 361–366 (2011).
18. D. A. Bandurin *et al.*, Resonant terahertz detection using graphene plasmons. *Nat. Commun.* **9**, 5392 (2018).
19. A. V. Muravjov *et al.*, Temperature dependence of plasmonic terahertz absorption in grating-gate gallium-nitride transistor structures. *Appl. Phys. Lett.* **96**, 042105 (2010).
20. K. Tantiwanichapan *et al.*, Graphene terahertz plasmons: A combined transmission spectroscopy and Raman microscopy study. *ACS Photonics* **4**, 2011–2017 (2017).
21. E. Hendry *et al.*, Optical control over surface-plasmon-polariton-assisted THz transmission through a slit aperture. *Phys. Rev. Lett.* **100**, 123901 (2008).
22. L. Ju *et al.*, Photoinduced doping in heterostructures of graphene and boron nitride. *Nat. Nanotechnol.* **9**, 348–352 (2014).
23. G. X. Ni *et al.*, Ultrafast optical switching of infrared plasmon polaritons in high-mobility graphene. *Nat. Photonics* **10**, 244–247 (2016).
24. A. A. Burkov, M. D. Hook, L. Balents, Topological nodal semimetals. *Phys. Rev. B Condens. Matter Mater. Phys.* **84**, 235126 (2011).
25. N. P. Armitage, E. J. Mele, A. Vishwanath, Weyl and Dirac semimetals in three-dimensional solids. *Rev. Mod. Phys.* **90**, 015001 (2018).
26. S. Das Sarma, E. H. Hwang, Collective modes of the massless Dirac plasma. *Phys. Rev. Lett.* **102**, 206412 (2009).
27. Z. Shi *et al.*, Observation of a Luttinger-liquid plasmon in metallic single-walled carbon nanotubes. *Nat. Photonics* **9**, 515–519 (2015).
28. J. Wang *et al.*, Anomalous Dirac plasmons in 1D topological electrides. *Phys. Rev. Lett.* **123**, 206402 (2019).
29. J. Wang *et al.*, Pseudo Dirac nodal sphere semimetal. *Phys. Rev. B* **98**, 201112(R) (2018).
30. A. Wixforth, M. Sundaram, K. Ensslin, J. H. English, A. C. Gossard, Dimensional resonances in wide parabolic quantum wells. *Phys. Rev. B* **43**, 10000(R) (1991).
31. Y. Wang, E. W. Plummer, K. Kempa, Foundations of plasmonics. *Adv. Phys.* **60**, 799–898 (2011).
32. J. Voit, One-dimensional Fermi liquids. *Rep. Prog. Phys.* **58**, 977–1116 (1995).
33. L. Gao *et al.*, Epitaxial growth of honeycomb monolayer CuSe with Dirac nodal line fermions. *Adv. Mater.* **30**, e1707055 (2018).
34. B. Liu *et al.*, Flat AgTe honeycomb monolayer on Ag(111). *J. Phys. Chem. Lett.* **10**, 1866–1871 (2019).
35. C. Zhong *et al.*, Two-dimensional honeycomb borophene oxide: Strong anisotropy and nodal loop transformation. *Nanoscale* **11**, 2468–2475 (2019).
36. J.-L. Lu *et al.*, Two-dimensional node-line semimetals in a honeycomb-Kagome lattice. *Chin. Rev. Lett.* **34**, 057302 (2017).
37. B. Feng *et al.*, Experimental realization of two-dimensional Dirac nodal line fermions in monolayer Cu_2Si. *Nat. Commun.* **8**, 1007 (2017).
38. B. Yang, X. Zhang, M. Zhao, Dirac node lines in two-dimensional Lieb lattices. *Nanoscale* **9**, 8740–8746 (2017).
39. C. Niu *et al.*, Two-dimensional topological nodal line semimetal in layered X_2Y (X = Ca, Sr, and Ba; Y = As, Sb, and Bi). *Phys. Rev. B* **95**, 235138 (2017).
40. H. Yan *et al.*, Damping pathways of mid-infrared plasmons in graphene nanostructures. *Nat. Photonics* **7**, 394–399 (2013).
41. A. K. Geim, I. V. Grigorieva, Van der Waals heterostructures. *Nature* **499**, 419–425 (2013).
42. K. S. Novoselov, A. Mishchenko, A. Carvalho, A. H. Castro Neto, 2D materials and van der Waals heterostructures. *Science* **353**, aac9439 (2016).
43. N. Hamada, Si. Sawada, A. Oshiyama, New one-dimensional conductors: Graphitic microtubules. *Phys. Rev. Lett.* **68**, 1579–1581 (1992).
44. S. Wang *et al.*, Logarithm diameter scaling and carrier density independence of one-dimensional luttinger liquid plasmon. *Nano Lett.* **19**, 2360–2365 (2019).

45. R. Saito, G. Dresselhaus, M. S. Dresselhaus, *Physical Properties of Carbon Nanotubes* (Imperial College Press, London, 1998).
46. K. Andersen, K. S. Thygesen, Plasmons in metallic monolayer and bilayer transition metal dichalcogenides. *Phys. Rev. B Condens. Matter Mater. Phys.* **88**, 155128 (2013).
47. F. H. da Jornada, L. Xian, A. Rubio, S. G. Louie, Universal slow plasmons and giant field enhancement in atomically thin quasi-two-dimensional metals. *Nat. Commun.* **11**, 1013 (2020).
48. S. Zhao *et al*., Correlation of electron tunneling and plasmon propagation in a luttinger liquid. *Phys. Rev. Lett.* **121**, 047702 (2018).
49. G. Kresse, J. Furthmüller, Efficient iterative schemes for ab initio total-energy calculations using a plane-wave basis set. *Phys. Rev. B Condens. Matter* **54**, 11169–11186 (1996).
50. P. E. Blöchl, Projector augmented-wave method. *Phys. Rev. B Condens. Matter* **50**, 17953–17979 (1994).
51. J. P. Perdew, K. Burke, M. Ernzerhof, Generalized gradient approximation made simple. *Phys. Rev. Lett.* **77**, 3865–3868 (1996).
52. I. Souza, N. Marzari, D. Vanderbilt, Maximally localized Wannier functions for entangled energy bands. *Phys. Rev. B Condens. Matter Mater. Phys.* **65**, 035109 (2001).
53. G. D. Mahan, *Many-Particle Physics* (Plenum Press, New York, 1990).
54. S. Poncé, E. R. Margine, C. Verdi, F. Giustino, EPW: Electron–phonon coupling, transport and superconducting properties using maximally localized Wannier functions. *Comput. Phys. Commun.* **209**, 116–133 (2016).
55. P. Giannozzi *et al*., QUANTUM ESPRESSO: A modular and open-source software project for quantum simulations of materials. *J. Phys. Condens. Matter* **21**, 395502 (2009).